The Astrophysical Journal, 997:47 (13pp), 2026 January 20 https://doi.org/10.3847/1538-4357/ae1ef8

The Relation between AGN and Host Galaxy Properties in the JWST Era. II. The Merger-driven Evolution of Seyferts at Cosmic Noon

Nina Bonaventura[1], George H. Rieke[1], Jianwei Lyu (吕建伟)[1], Andrew J. Bunker[2], Chris J. Willott[3], and Christopher N. A. Willmer[1]
[1] Steward Observatory, University of Arizona, 933 North Cherry Avenue, Tucson, AZ 85721, USA; nbonaventura@arizona.edu
[2] Department of Physics, University of Oxford, Denys Wilkinson Building, Keble Road, Oxford OX1 3RH, UK
[3] NRC Herzberg, 5071 West Saanich Road, Victoria, BC V9E 2E7, Canada
Received 2025 August 27; revised 2025 November 1; accepted 2025 November 9; published 2026 January 13

Abstract

In Paper I, we exploited the unsurpassed resolution and depth of JWST/NIRCam imagery to investigate the relationship between active galactic nuclei (AGN) and host-galaxy properties in the JWST era, finding a correlation between the level of spatial disturbance (as measured by shape asymmetry, A_S) and obscuration (N_H). Here in Paper II, we report an expansion of our X-ray and infrared analysis of Seyfert-luminosity host galaxies with four additional metrics to the single-metric morphology analysis of Paper I, as well as new samples of inactive control galaxies. This expanded study of one of the largest and most complete, multiwavelength samples of AGN detected at $0.6 < z < 3.8$ in the GOODS-South and -North fields, confirms that mergers surprisingly play a significant role in obscured, subquasar AGN host galaxies. Additionally, the pattern of morphological disturbances observed amongst the X-ray- and mid-IR-selected AGN suggests that these represent different phases of AGN evolution tied to a major-merger timeline, as opposed to distinct populations of AGN. These results indicate that mergers are important in triggering subquasar AGN at these redshifts.

Unified Astronomy Thesaurus concepts: AGN host galaxies (2017)

1. Introduction

The role of galaxy mergers in triggering and feeding active galactic nuclei (AGN) is a central prediction of a number of theoretical simulations, but has been difficult to demonstrate observationally. The numerous investigations into this suspected AGN–merger connection have not converged on a solid result, as discussed, for example, in the review by C. Villforth (2023; see also, e.g., Y. Zhao et al. 2022; K. C. Omori et al. 2025). However, as studies have moved from selections favoring lightly obscured AGN (through optical colors, broad emission lines, and X-ray detection) to those inclusive of heavier obscuration (typically sources faint in the optical and/or X-ray), this picture has changed; nearly every study of obscured AGN has found that they tend to reside in galaxy mergers (D. D. Kocevski et al. 2015; C. Ricci et al. 2017; M. E. Weston et al. 2017; J. L. Donley et al. 2018; A. D. Goulding et al. 2018; S. L. Ellison et al. 2019; R. W. Pfeifle et al. 2019; F. Gao et al. 2020; R. S. Barrows et al. 2023; D. Kim et al. 2024; N. Bonaventura et al. 2025, hereafter, Paper I; Euclid Collaboration et al. 2025).

In general, these results have been confined to very luminous AGN, in part because Wide-field Infrared Survey Explorer (WISE; E. L. Wright et al. 2010) infrared data have played a key role in identifying obscured AGN: the spectral energy distributions (SEDs) of WISE-detected AGN, by definition, require a relatively high AGN luminosity to appear against the competing emission from the host galaxy in this portion of the SED (R. C. Hickox & D. M. Alexander 2018).

The theoretical expectation has been that lower-luminosity AGN, unlike quasars, can passively grow through stochastic processes without being associated with mergers (e.g., P. F. Hopkins & L. Hernquist 2006, 2009; S. McAlpine et al. 2018; A. K. Weigel et al. 2018, and references therein). However, before the advent of JWST, it was difficult to investigate the role of mergers in the triggering and evolution of obscured, lower-luminosity AGN, as there were no mid-infrared surveys with adequate sensitivity and wavelength coverage to yield a significant sample of such AGN. Furthermore, it was difficult to obtain detailed rest-optical (observed near-infrared) morphologies of high-redshift galaxies hosting moderate-luminosity AGN, due to limited observing capability in this wavelength range, and the inability of JWST's predecessors to overcome the surface brightness dimming caused by cosmological expansion (e.g., Y. Shi et al. 2009). This issue drove studies to probe the frequencies and characteristics of obvious mergers, where two galaxies or two nuclei appear, rather than morphological indications of disturbance in single galaxies (i.e., candidates for merger remnants; E. A. Shah et al. 2020).

Consequently, it is possible that late postcoalescent merger remnants have been frequently overlooked and misclassified as nonmergers, and therefore excluded from merger studies, given that the telltale signatures of postcoalescence, such as tidal tails, wisps, and cusps around the galaxy edge, would typically have been too faint to be observed.

In Paper I, the superior sensitivity and resolution of JWST/NIRCam enabled the discovery of strong galaxy-scale spatial disturbances in a significant fraction of our AGN sample at $z > 0.5$, which was unexpected given that subquasar AGN are thought to be triggered predominantly by nonmerger mechanisms. This finding suggests that merger signatures persist in remnants for longer than previously thought (e.g., S. Ellison et al. 2025), and that Seyfert activity is enhanced significantly

with the pervasive merging found to occur at Cosmic Noon (e.g., C. J. Conselice et al. 2022; D. Puskás et al. 2025).

Another key component of our analysis that allowed for the detection of significant evidence of prior merging activity in our AGN sample was our use of the shape asymmetry (A_S) parameter in diagnosing merging morphologies in imaging data (M. M. Pawlik et al. 2016; R. Nevin et al. 2019). This nonparametric morphology indicator provides a clean and unbiased measure of the level of spatial disturbance along the edges of a galaxy by using the binary detection image corresponding to its flux image—meaning it is uninfluenced by brightness asymmetries unrelated to merging activity, unlike the classic asymmetry parameter, A.

In the current study, in addition to comparing the AGN host morphologies to a new sample of 784 matched inactive (non-AGN) control galaxies, we build upon the results of Paper I by continuing our analysis of 425 AGN selected at X-ray and mid-IR wavelengths from $z \sim 0.5$ to $z \sim 4$ in the following ways:

(1) We expand the AGN host-galaxy morphology analysis to encompass four additional metrics to the shape asymmetry reported in Paper I, allowing us to distinguish disturbances caused by major versus minor mergers and therefore assign a statistically likely merger type to each AGN in the sample. This additional information allows us to determine if merging activity in Seyferts is significant to their evolution and SMBH growth, as would be indicated by significant evidence of major-merging activity.
(2) We investigate if the SED-derived properties of the mid-IR and X-ray AGN host galaxies support the results of the morphology analysis: that these two subsamples are not distinct AGN classes, but likely different phases of an AGN evolutionary sequence, where the mid-IR/X-ray-faint phase chronologically precedes the X-ray-bright phase and occurs closer in time to the statistically likely major merger that drives their evolution.
(3) We investigate if the conclusion we draw from the combined morphology and SED analysis of this representative sample of Seyferts holds up in comparison to control samples of non-AGN galaxies matched on stellar mass, redshift, specific star formation rate (sSFR), and selection wavelength.

As in Paper I, we adopt the cosmology of the studies from which we draw our AGN sample, namely J. Lyu et al. (2022) and J. Lyu et al. (2024), who adopt a slightly different cosmology: J. Lyu et al. (2022) assume $\Omega_m = 0.27$ and $H_0 = 71$ km s^{-1} Mpc^{-1}, and J. Lyu et al. (2024) assume $\Omega_m = 0.287$ and $H_0 = 69.3$ km s^{-1} Mpc^{-1}. This minor difference does not affect the conclusions of our study.

2. Samples and Data

In the present study we extend our analysis of the primary AGN sample considered in Paper I, which is comprised of two subsamples: (1) 243 X-ray-selected AGN analyzed in J. Lyu et al. (2022; GOODS-S) and J. Lyu (2025, private communication, GOODS-N); and (2) 182 mid-infrared (mid-IR)-selected AGN analyzed in J. Lyu et al. (2024; GOODS-S), for a total of 425 AGN.

In Paper I, in addition to the full primary sample, we analyzed a subset consisting of only those X-ray and mid-IR AGN matched on various source properties, to rigorously quantify a relationship between AGN obscuration and spatial disturbance. Here, we consider the full, unmatched primary sample, at the redshifts where it is complete ($0.5 < z < 3.8$), to uncover a suspected relationship between the X-ray and mid-IR AGN.

2.1. X-Ray AGN Sample

The X-ray AGN sample consists of 243 lightly to highly obscured Chandra-detected sources lying at redshifts $0.5 < z < 3.8$, with $N_{\rm H}$ values in the range 10^{22}–10^{24} cm^{-2}, as derived from hardness ratios (T. Liu et al. 2017; B. Luo et al. 2017). Their stellar masses[4] (M_*) and bolometric luminosities ($L_{\rm bol}$) are estimated from the SED-fitting procedure described in J. Lyu et al. (2022) and lie in the range 10^{9}–$10^{11.5}\,M_\odot$ and 10^{41}–10^{46} erg s^{-1}, respectively. A description of the full set of properties relevant to this study is contained in Paper I.

2.2. Mid-IR AGN Sample

The mid-IR AGN sample was relatively recently identified with the Systematic Mid-infrared Instrument Legacy Extragalactic Survey (SMILES; J. Lyu et al. 2024) and consists of many highly obscured (X-ray-faint) systems, 80% of which were previously undetected by extensive pre-JWST AGN searches in GOODS-S (J. Lyu et al. 2024). We include 182 AGN in our analysis with the following SED-derived properties: $10^9 \leqslant M_*/M_\odot \leqslant 10^{11.4}$, $10^{42} \leqslant L_{\rm bol} \leqslant 10^{46}$, and $0.5 < z < 3.8$. These sources were classified as AGN through an SED analysis making use of 27 photometric bands, including 5 HST/ACS bands (0.44–0.9 μm), 14 JWST/NIRCam bands (0.9–4.4 μm), and 8 JWST/MIRI bands (5.6–25.5 μm; J. Lyu et al. 2024). A description of the full set of properties relevant to this study is contained in Paper I.[5]

2.3. Inactive Control Samples

To determine if the morphology patterns we observe in our AGN sample are unique to AGN, and therefore that we are truly uncovering an evolutionary mechanism in Seyferts at Cosmic Noon, we repeated the full host-galaxy morphology analysis of Paper I on a control sample of inactive galaxies. We collected three different control samples to (1) guard against unsuspected systematic effects that might plague a single sample; (2) be as comprehensive as possible in the property-matching to the different AGN subsamples by matching on selection wavelength; and (3) to maximize the number of inactive controls for better statistics.

[4] The stellar-mass estimates are inferred from stellar-population-synthesis modeling with the *Prospector* code, and the AGN component has been modeled by a set of well-tested, semiempirical templates (see J. Lyu et al. 2024 for details). We note that the vast majority of the galaxies in our sample have highly obscured AGN; therefore, AGN contamination is not expected to impact their M_* estimates, as demonstrated by L. Ciesla et al. (2015).

[5] We note that our mid-IR AGN sample is fundamentally different from previous "IR AGN" samples that were selected on the basis of Spitzer/IRAC or WISE infrared colors: as is shown in J. L. Donley et al. (2012), these color-selection methods reveal AGN SEDs described by a power-law model, which means that at significant redshift, the power-law shifts into the near-infrared. Thus, IR AGN selected according to this method are *not* heavily embedded, but instead are moderately obscured, Type-1 AGN. In comparison, our sample was detected on account of the significantly improved sensitivity and continuous spectral coverage of JWST/MIRI.

2.3.1. Near-IR-selected Inactive Galaxies

For the primary inactive control sample, we utilized the stellar-mass catalog for the GOODS-S field detailed in P. Santini et al. (2014), which was selected using deep near-IR HST photometry as part of the Cosmic Assembly Near-infrared Deep Extragalactic Legacy Survey (CANDELS) project; these masses were derived from SED template fitting constrained by ∼10 photometric bands (A. Grazian et al. 2006). From this catalog, we extracted sources that were not flagged as AGN or stars, that have stellar masses[6] in the $9 < \log(M_*/M_\odot) < 11$ range and SFR $< 100\,M_\odot\,\mathrm{yr}^{-1}$[7], and that have SNR $\geqslant 30$ at $0.5 < z < 3.0$ and SNR $\geqslant 10$ at $3.0 < z < 4.0$ (to boost the number of sources selected at highest redshifts, where fewer sources were available than at lower redshifts). This resulted in a sample of 529 control galaxies.

2.3.2. Mid-IR-Selected Inactive Galaxies

The second inactive control sample was chosen to match the mid-IR AGN subsample, and therefore was drawn from the same MIRI SMILES catalog and analyzed using the identical SED analysis as the AGN sources in the catalog. We required these sources to be classified as non-AGN, with an SFR less than $100\,M_\odot\,\mathrm{yr}^{-1}$ (which also limited $L_{\mathrm{IR}} < 10^{12}\,L_\odot$), and with stellar masses ($9 < \log(M_*/M_\odot) < 11$) and redshifts ($z < 4$) matched to the mid-IR AGN. We found 213 such inactive control galaxies that were included in the JWST Advanced Deep Extragalactic Survey (JADES) NIRCam v1 mosaic image used for morphology analysis.

2.3.3. X-Ray-selected Inactive Galaxies

The third inactive control sample was drawn from the X-ray source catalog of B. Luo et al. (2017), which contains information on hundreds of X-ray-identified sources within the 3D-HST footprint and therefore overlaps with our X-ray-selected AGN sample in GOODS-S. The list of inactive control galaxies was gathered by first identifying those in the catalog designated as non-AGN, and then further filtering from that list the lingering AGN contaminants using the superior AGN detection methods of J. Lyu et al. (2022). Next, we calculated the stellar masses of the non-AGN from their observed K_s magnitudes and then matched to the X-ray AGN sample on stellar mass and redshift. Finally, we removed those galaxies found to lie outside the footprint of the JADES NIRCam v1 mosaic imagery used for morphological analysis, leaving 42 X-ray-selected inactive control galaxies. While the X-ray source catalog of B. Luo et al. (2017) does not provide estimates of SFR, B. D. Lehmer et al. (2016) find that 96% of the non-AGN in this sample have SFR $< 100\,M_\odot\,\mathrm{yr}^{-1}$, and therefore our X-ray AGN and control samples are also matched on SFR.

We note that, unlike for the near-IR and mid-IR control samples, the ranges of both redshift and stellar mass on which the X-ray control sample could be matched to the X-ray AGN are smaller than the full redshift ($0.5 < z < 4$) and stellar-mass range ($9 < \log(M_*/M_\odot) < 11$) of the primary X-ray AGN sample, as shown in the bottom plot of Figure 1.

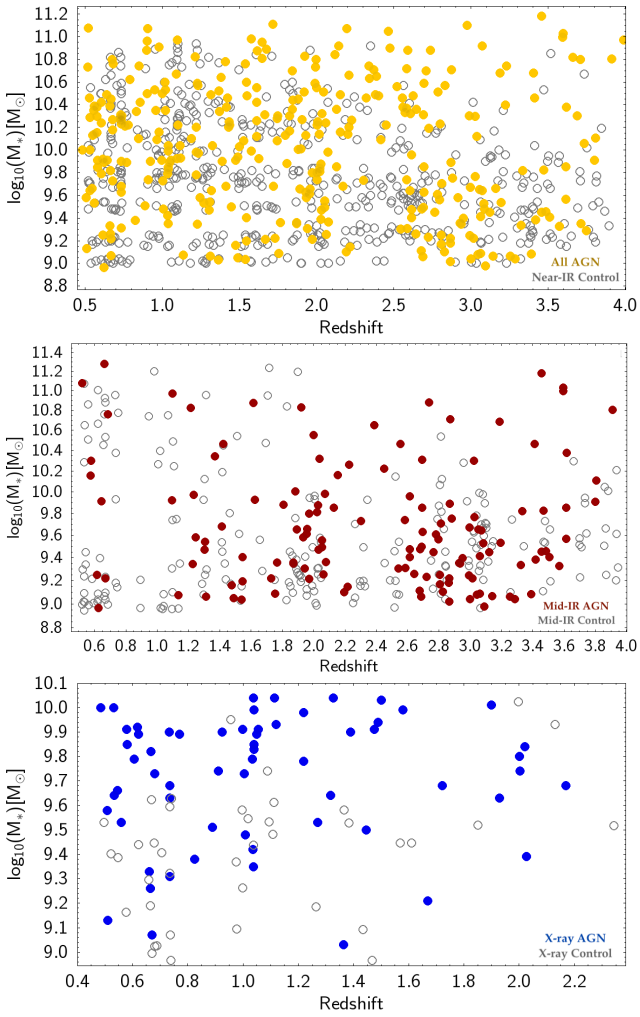

Figure 1. The distributions of the stellar masses and redshifts of the inactive control samples matched to the AGN sample. The top figure shows the near-IR-selected control sample from CANDELS with the full primary AGN sample in yellow. The middle figure shows the mid-IR AGN (red) and corresponding MIRI-selected control sample. The bottom figure shows the X-ray AGN (blue) compared to the X-ray-selected control sample.

2.4. JWST NIRCam Data

As in Paper I, for the AGN host-galaxy morphological analysis, we utilize the NIRCam F150W mosaic imagery from version 1 of the JADES. This survey is introduced in JWST programs 1180 and 1181 (PI: Eisenstein), and fully described in the JADES Data Release v1 paper (M. J. Rieke et al. 2023) and JWST Extragalactic Medium-band Survey (JEMS; JWST PID 1963) paper (C. C. Williams et al. 2023). Each mosaic image achieves $0\farcs03\,\mathrm{pixel}^{-1}$ resolution and an AB magnitude depth of 29–30 (M. J. Rieke et al. 2023).

3. Methodology

3.1. Characterizing AGN Obscuration

Our sample is selected on the basis of X-ray and infrared properties and is almost entirely obscured, i.e., of type S1.8 - S2, or Compton-thick, according to the usual identification of obscured AGN as those with $\log(N_{\mathrm{H}}) > 22$ (e.g., G. Risaliti

[6] The stellar-mass catalog in P. Santini et al. (2014) contains 10 different M_* estimates; we utilized the 11a$_\tau$ method, described in Section 3.2 of that paper. This method utilizes the G. Bruzual & S. Charlot (2003) stellar templates, a Chabrier IMF, and an exponentially decreasing SFH (direct-τ model).

[7] M. K. Florian et al. (2025) demonstrate insignificant morphological disturbance in this range of SFR.

et al. 1999; P. Padovani et al. 2017; E. S. Kammoun et al. 2020; A. Annuar et al. 2025). As shown in the line-of-sight (LOS) X-ray absorption distribution in Figure 1 of Paper I, the sample contains very few examples at $\log(N_{\rm H}) < 22$, with most lying in the $22 < \log(N_{\rm H}) < 24+$ range. This sampling will typically have obscured nuclei in the optical (e.g., L. Burtscher et al. 2016; P. Padovani et al. 2017), leading to low contrast against the stellar population of the galaxy—a prediction that agrees well with visual inspection of our sample (see the examples in Figure 2 and in Figure 3 of Paper I). We have therefore conducted the morphological analysis without correcting for a central point source, given that only a very small fraction of the galaxies under study exhibit one. Our approach is supported by the accuracy of the nucleus/galaxy deconvolutions for Type 2 AGN demonstrated in L. Ciesla et al. (2015).

3.1.1. N_H Measurements

The values for $N_{\rm H}$ that we adopted for our X-ray AGN sample, obtained from B. Luo et al. (2017) and T. Liu et al. (2017), are not provided with individual error estimates; however, the typical error estimates presented in K. V. Getman et al. (2010) show ∼0.2–0.3 dex for the faint sources that dominate our sample. Another source of error in the obscuration is that we use LOS $N_{\rm H}$ as a proxy for isotropic obscuration, whereas there will be variations in the obscuration over 4π steradians around the source; this is a relatively complex effect and is discussed in the Appendix. The conclusion is that $N_{\rm H}$ has proven to be a reliable proxy of isotropic obscuration despite these variations, i.e., even if the LOS intersects an unusually thin or thick region of obscuration and results in an under- or overestimate of the overall obscuration level.

3.2. Multimetric Merger Morphology Analysis

In Paper I, we relied on the shape asymmetry parameter (A_S) to identify merger signatures in imaging data, following the procedures developed by R. Nevin et al. (2019; hereafter "N19"). Those authors simulated SDSS *r*-band images of local, major- and minor-merging galaxies, and used statmorph (V. Rodriguez-Gomez et al. 2019) to generate a large statistical sample of their nonparametric morphology measurements; they then fit those parameters together in a linear discriminant analysis (LDA) that proved to robustly diagnose merging morphology in imaging data. From that study, it became apparent that A_S individually outperforms the other metrics in diagnosing merger signatures in imaging data (as was also shown in M. M. Pawlik et al. (2016), where A_S was introduced), and over the longest length of the merger timeline—only surpassed by the LDA diagnostic that combines all morphology metrics considered in their study. Therefore, A_S dominates the calculations used in N19 to quantitatively classify merger signatures in images. In R. Nevin et al. (2023, N23), the authors expand and refine the LDA analysis to robustly distinguish major from minor mergers, as well as to identify merger stage.

As introduced in N19, the imaging component of the LDA framework performs a supervised classification of merging versus nonmerging galaxies by identifying the linear combination of morphological features that separates them (Equations (1) and (2) of N23), including A_S, the Gini coefficient, the M_{20} statistic, concentration (C), asymmetry (A), clumpiness (S), and Sérsic index (n):

$$\begin{aligned}\mathrm{LD1}_{\rm major} = &+13.9A_s - 8.0C * A_s - 5.4A * A_s + 5.1A \\ &+ 4.8C - 2.9\mathrm{Gini} * A_s + 0.6M_{20} * A \\ &+ 0.4M_{20} * n + 0.4\mathrm{Gini} - 0.6\end{aligned}$$

$$\begin{aligned}\mathrm{LD1}_{\rm minor} = &-10.4\mathrm{C} * A_s + 8.8\mathrm{C} * A - 7.8\mathrm{Gini} * S - 7.8A \\ &+ 6.6A_s + 6.5\mathrm{Gini} * M_{20} - 6.0M_{20} * S \\ &- 5.7M_{20} * A_s + 4.9\mathrm{S} - 4.4M_{20} + 3.7\mathrm{Gini} * C \\ &- 2.9\mathrm{S} * n - 1.0n * A_s - 0.2A * S - 0.7.\end{aligned}$$

The results of N19 showed that their LDA method, which considers seven different morphology metrics, outperforms

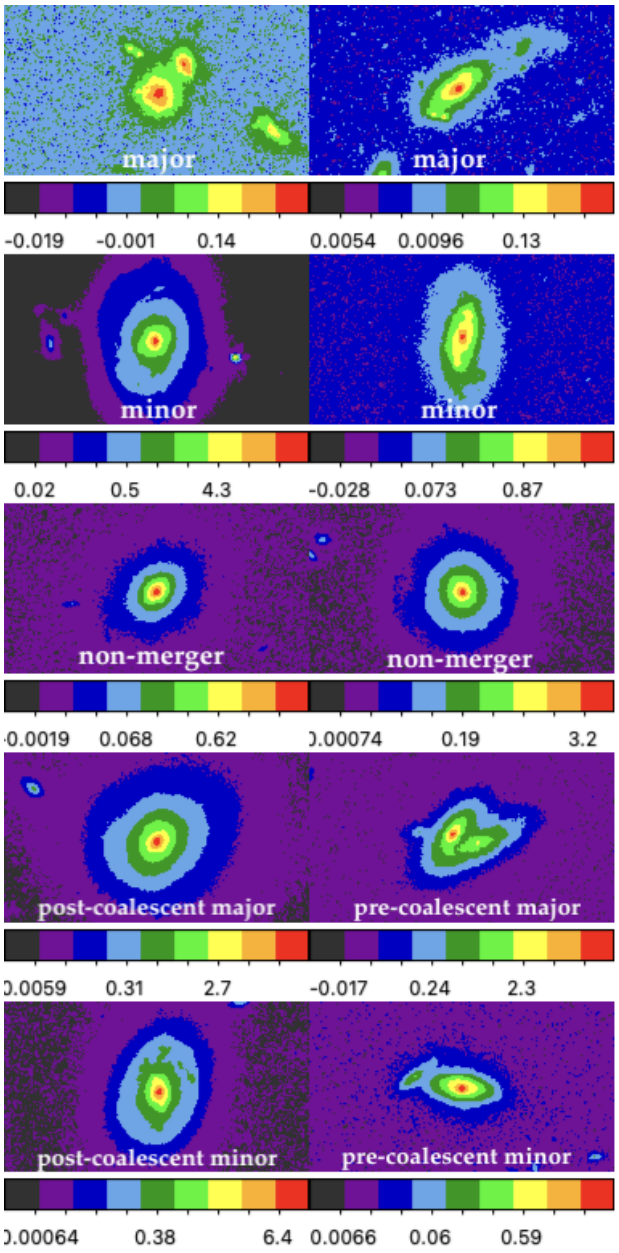

Figure 2. Examples of AGN host galaxies that were classified as major, minor, and nonmergers by the combined major/minor-merger classifications shown in Table 1, used to diagnose the likely merger stage corresponding to the spatial asymmetries uncovered in Paper I. Additionally, we show examples with the full set of morphology indicators required for a further refinement of the classification to merger stage. These images were cut from the F150W NIRCam v1 mosaics used for morphology characterization in the current paper and Paper I, with pixel intensities colored with SAOImage "aips0" and shown on a log scale.

Table 1
Linear Discriminant Analysis Metrics for Merger Classification

Classification	Term 1	Term 2	Term 3	Term 4
All major mergers	$13.9 \pm 1.0A_s$	$-8.0 \pm 0.7A_s * C$	$-5.4 \pm 0.4A_s * A$	$5.1 \pm 0.4A$
Major, pre-coalescence	$10.0 \pm 0.6A_s$	$7.5 \pm 0.2A$	$-6.3 \pm 0.2A_s * A$	$-6.1 \pm 0.5A_s * C$
Major, early stage	$9.1 \pm 0.4A_s$	$-5.8 \pm 0.4A_s * C$	$5.3 \pm 0.6C$	$4.9 \pm 0.5A$
Major, late stage	$-8.9 \pm 0.8A_s * A$	$7.9 \pm 0.4A_s$	7.2 $\pm$ 0.7 Gini $*$ A	$1.2 \pm 0.2A * S$
Major, postcoalescence (1.0 Gyr)	$-14.3 \pm 0.9C * n$	$11.7 \pm 1.4C$	5.9 $\pm$ 0.9 Gini $*$ n	$-1.3 \pm 0.2A_s * M_{20}$
All minor mergers	$-10.4 \pm 1.9A_S * C$	$8.8 \pm 0.7A * C$	$-7.8 \pm$ 3.3 Gini $*$ S	$-7.8 \pm 0.6A$
Minor, pre-coalescence	-31.3 ± 7.7 Gini $*$ S	$-28.6 \pm$ 6.0 Gini $*$ n	$27.4 \pm 5.7n$	$21.0 \pm 2.8C$
Minor, early stage	$20.8 \pm 3.6C$	-20.5 ± 5.4 Gini $*$ C	$-18.0 \pm 2.2n * M_{20}$	$-16.7 \pm 2.2n * C$
Minor, late stage	$10.1 \pm 1.4A_s * C$	$-5.3 \pm 1.0A_s *$ Gini	$1.9 \pm 0.1A_s * A$	⋯
Minor, postcoalescence (1.0 Gyr)	2.0 ± 0.1 Gini	$-1.1 \pm 0.1A * S$	$0.6 \pm 0.1n$	⋯

Note. The morphology predictors used here are standardized values based on the mean and standard deviation of each classification.
In our final analysis, we utilized only the combined major/minor-merger classifications shown, as the Gini and/or Sérsic n values required for most of the other classification metrics were unusable for a significant fraction of our sample, as discussed in the text.
Please see Table 2 of R. Nevin et al. (2023) for the classification of host-galaxy merger type and stage, where the four leading coefficients and terms dictating each merger classification are shown, based on the corresponding fit to the full set of galaxy morphology parameters (noting the removal of the 0.5 Gyr postcoalescence classifications, as they show lower performance statistics than the 1.0 Gyr postcoalescence classifications; see Section 4.3 of N23 for details).

popular merger classification methods such as the Gini $- M_{20}$ diagnostic and the use of A or A_S alone. In N23, the LDA classifier is used to identify merging galaxies of varying mass ratios (major versus minor) as well as merger stage (early, late, postcoalescent), in a sample of 1.34 million local SDSS galaxies.

To expand upon the AGN host-galaxy morphology analysis of Paper I to encompass a broader set of morphology metrics, and therefore determine the merger type and stage indicated by the shape asymmetries of Paper I, we again used statmorph to generate the full set of morphology measurements required to conduct the LDA analysis. As in N23, we classified our galaxy sample according to the four leading coefficients and terms for each of the merger type and stage classifications contained in Table 1.

The predictor values (as they are referred to in N19 and N23) we measured for each morphology parameter for the AGN hosts were consistent with the distributions of those measured for the local SDSS galaxies (see Figure 1 of N23), for all but the most heavily obscured systems;[8] therefore, we directly applied the N23 LDA model to our NIRCam data. In other words, we did not simulate JWST/NIRCam images of galaxies and then refit to this data the LDA model of N23 to tune the parameters accordingly, as we consider their model to be generalizable to NIRCam data: the only instrumental difference we expect to manifest in our NIRCam images is a higher SNR than the simulated SDSS images, despite the higher redshifts we probe (see Figure 11 of Paper I for a comparison of a sample of our real NIRCam images to their simulated SDSS galaxies at matched rest-frame wavelength).

Given that the Gini and/or n metrics required for refining the classification of merger type into merger stage were not available or valid for a significant fraction of our sample, we utilized only the combined major/minor-merger LDA metrics for determining merger type, using the four leading coefficients and terms of Equations (1) and (2) (also shown in Table 1) as in N23. Where the Gini coefficient values were invalid (for the N23 analysis) for the most-obscured AGN (41% of the sample), we could not classify those galaxies as minor mergers, due to the dependence of the minor-merger classification metric on Gini. However, all strongly classify as major mergers at 98.2% $\pm$ 5.6%; therefore, we assume these AGN to be associated with major mergers.

In our analysis, to qualify as a major-merger candidate, the probability value ($p_{\rm merg} = 1/(1 + e^{-LD1})$) resulting from the LDA classification for major mergers was required to be greater than 0.5, while the probability value associated with the minor-merger classification for the same galaxy had to be less than 0.5 (and vice versa to classify a galaxy as a minor merger); see Figure 2 for examples. A low probability for both classifications indicates a nonmerger classification. The relatively small fraction (6.8%) of galaxies with degenerate merger type classifications, i.e., those with LDA values suggesting a high probability of being both major and minor (probabilities greater than 0.5 in both cases), were simply labeled as a "merger" to indicate an inability to distinguish the merger type (these are included in the total merger fractions plotted in the top panel of Figure 3). Furthermore, despite the fact that we excluded from our final analysis the N23 LDA classifications for merger stage, we confirmed in Paper I that nearly all AGN in our sample are isolated, as indicated by a lack of a companion galaxy within 50 kpc at the same redshift that would indicate a precoalescent merger stage. Therefore, we assume that the merger candidates we identify are in the

[8] We learned during this analysis that the Gini coefficient values measured for our Compton-thick (CT) AGN lie outside the parameter space of the SDSS galaxies, indicating a new area of exploration for very heavily obscured examples not included in the N23 study. We also observed for our most-obscured AGN, that the Sérsic fitting failed because the CT AGN are the most spatially disordered, and therefore we could not in those instances obtain a measure of the Sérsic index required for a number of the merger classification formulae in N23. In future work, we plan to conduct a similar analysis to N23 to explore this new parameter space for highly obscured galaxies observed in JWST data.

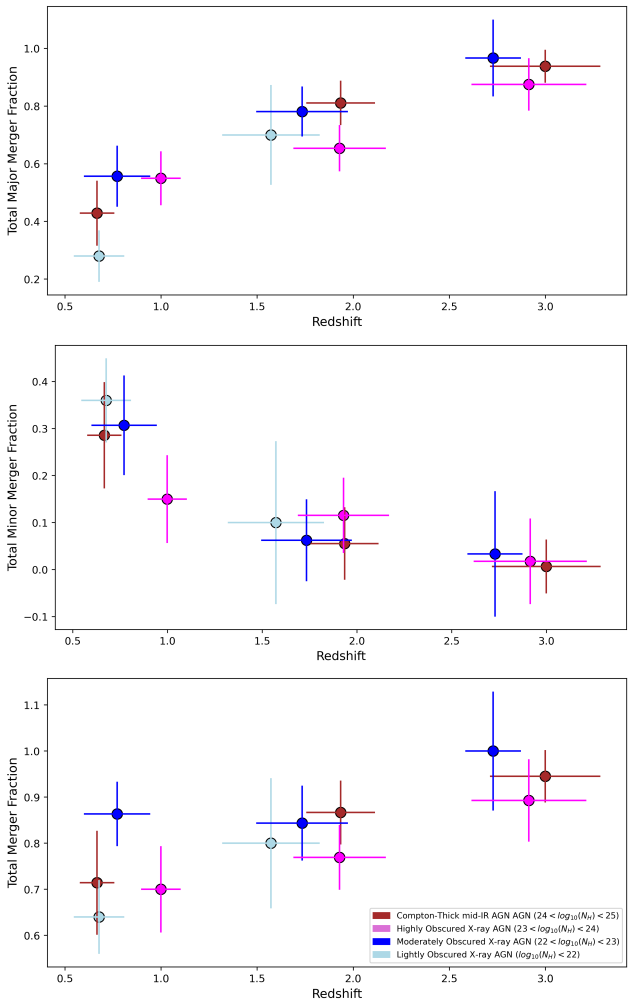

Figure 3. The major, minor, and total merger fractions resulting from the N23 LDA analysis of our primary AGN sample as a function of redshift (x-axis) and $N_{\rm H}$ (point color, simulated for CT mid-IR AGN shown in dark red). We observe a rising (decreasing) fraction of major (minor) merger candidates toward higher redshifts and an increasing total merger fraction with redshift, given that the majority of the merger candidates are classified as major mergers. Here we can see that the majority of the AGN sample exhibit the morphologies characteristic of a merger. (Not shown in the figure are the 8% of the sample classified as nonmergers, 6.8% with degenerate major/minor classifications, and 8% unidentifiable due to poor Sérsic profile fits.)

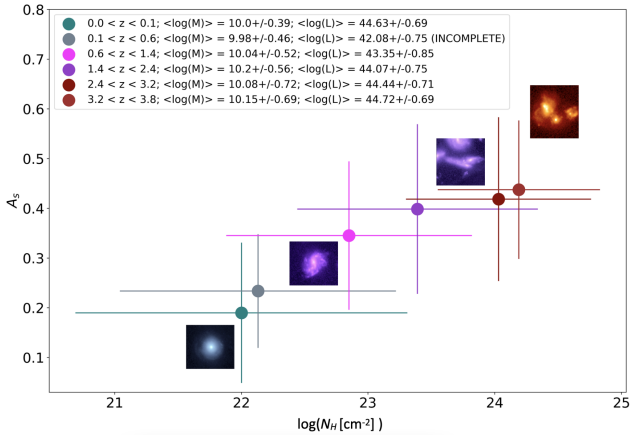

Figure 4. From Paper I, the trend in the shape asymmetry parameter A_S with $N_{\rm H}$ and redshift, where the primary AGN sample considered here is contained in the points for $0.6 < z < 3.8$. Here it can be seen that, at Cosmic Noon, the majority of AGN are significantly spatially disturbed and that, at the highest levels of $N_{\rm H}$ and redshift, the observation of spatial disorder (i.e., an irregular morphology type of a single galaxy or an obvious merger with multiple visible nuclei) in combination with high A_S indicates the early stages of a chaotic merger.

postcoalescent stage, minus the handful observed to be in the late merger stage with two visible nuclei.

The results of our LDA analysis are shown in Figure 3, where we see the fraction of AGN in minor and major mergers as a function of both redshift and $N_{\rm H}$ (where $N_{\rm H}$ has been simulated for the CT mid-IR AGN as described in Section 2.1.2 of Paper I). From this it is clear that the host galaxy disturbances in a majority of the AGN sample are likely to have been induced by a recent major merger, with an increasing major (decreasing minor) merger fraction observed toward higher redshift.

The results of multimetric morphology analysis therefore agree with the A_S analysis from Paper I, indicating that the strong spatial asymmetries characterizing the majority of the sample are likely to be the result of major mergers and that these are common among obscured Seyferts at Cosmic Noon. The multimetric analysis also appears to confirm our speculation from Paper I that Seyferts are unexpectedly evolving according to the cosmological merger rate like quasars, as evidenced by both the decreasing degree of host disturbance and number of hosts with disturbances observed at lower redshift. Figure 4 reveals the main findings of Paper I, that there is a trend in the type of disturbance with increasing obscuration, alongside the increase of spatial asymmetry: at the highest levels of $N_{\rm H}$, the galaxies are both more asymmetric and disordered than at lower levels, i.e., the host galaxies of the most heavily obscured AGN have more chaotic morphologies than the hosts of less obscured and presumably more evolved AGN.

It would appear that the widespread major merging occurring among Seyferts at Cosmic Noon ought to play a significant role in their triggering, while passive/secular processes begin to play an increasingly important role at lower redshifts (where the Seyfert characteristics were originally defined, and perhaps the main reason this class of AGN was not believed to be involved in mergers until now). The control sample morphology analysis, presented in Section 4, lends further support to these arguments.

3.3. Comparison of SED-derived AGN Host Galaxy Properties

To achieve the second goal of our follow-up analysis to Paper I, we compare the average SED-derived sSFRs and intrinsic X-ray luminosities of the X-ray-bright/mid-IR-faint and X-ray-faint/mid-IR-bright AGN subsamples to check for trends that would either support or contradict the implication that they are linked to a common evolutionary scenario. Given the faintness of the mid-IR AGN in X-rays, this portion of the analysis involved stacking the X-ray fluxes of the mid-IR AGN to (a) confirm their CT status that we only presumed in Paper I, proving they are in fact an extension of the X-ray-detected sample into the CT regime (given their otherwise similar host-galaxy properties); and (b) to enable a direct comparison of their estimated SMBH accretion rates to their X-ray counterparts via their stacked $L_{x,\rm int}$ (rest 0.5–7 keV) luminosities.

3.3.1. Stacked X-Ray Luminosities of the mid-IR AGN

For many of the most heavily obscured AGN, there has been little direct confirmation that they are truly AGN. While the mid-IR AGN sample was identified as such through a broadband SED analysis composed of HST and JWST data, we address that issue by showing that, as a group, they also have the expected X-ray properties for that designation (G. H. Rieke et al. 2025). This also enabled a comparison of the intrinsic X-ray luminosities and implied accretion rates of the X-ray AGN to the CT mid-IR/X-ray-faint AGN.

To generate stacked X-ray flux measurements of the CT mid-IR AGN, we utilized the CSTACK (T. Miyaji et al. 2008) software, which performs aperture photometry on an input list of sources, using archival Chandra ACIS-I observations (Cycle 15) in each of the soft (0.5–2 keV) and hard (2–8 keV) observed X-ray bands. For our analysis, we chose the deepest available Chandra data in CSTACK, namely the Chandra Deep Field South (CDFS) 7-Mega-Second survey, and stacked the mid-IR AGN in our GOODS-S sample in two redshift bins, $z = 1.2$–2.4 (19 AGN) and $z = 2.4$.–3.8 (68 AGN). The choice to explore the X-ray properties of the mid-IR AGN as a function of redshift was motivated by the thought that, if we are observing a previously unnoticed, fundamental characteristic of Seyfert evolution at Cosmic Noon, it should be observed consistently throughout the redshift bins of our analysis at $z > \sim 0.5$.

The stacked X-ray fluxes were calculated using the default/recommended CSTACK settings, where the circular apertures used to sum source counts correspond to an enclosed counts fraction of 0.9; and the background level in each image is estimated using a $30'' \times 30''$ square region centered on the source position, excluding the emission within a $7''$-radius around the source. Furthermore, to achieve the most accurate stacked fluxes, we allowed the software to employ its default criteria for automatically rejecting from the input source list those whose apertures were contaminated by flux from nearby resolved sources, as well as the sources that were themselves resolved and heavily influencing the stacked source count. The stacked count rate value calculated by CTSTACK represents a weighted and normalized mean of the rates for the accepted objects, with a corresponding uncertainty value calculated using a bootstrap resampling analysis, which is considered to be more accurate than simply using photon-counting statistics (see the CSTACK reference for further details). This procedure resulted in a significant stacked X-ray count rate in each redshift bin of the mid-IR AGN sample, in one or both of the soft and hard X-ray bands, confirming their status as the most heavily obscured, CT AGN of our full AGN sample.

To estimate the intrinsic, rest-frame 0.5–7 keV X-ray luminosity ($L_{x,\mathrm{int}}$) corresponding to the stacked X-ray count rate generated by CSTACK in the soft and hard X-ray bands, per redshift bin, we first calculated the corresponding physical flux value using the PIMMS v4.14 tool available in the Chandra Proposal Planning Toolkit. The PIMMS tool translates an input X-ray count rate, flux, or flux density value in a given energy range, specific to a chosen Chandra cycle and detector/grating/filter combination, into an output count rate, flux, or flux density value in the desired output energy range, using the input model parameters that describe the source emission. In other words, PIMMS interpolates the spectral model to the input parameters, folds it through (i.e., multiplies) the Chandra effective area curves, and integrates over the user-specified input energy band(s) to determine the appropriate conversion factors.

To model the CT AGN in PIMMS, we chose an absorbed power law with a photon index of 1.8; a Galactic N_{H} absorption value of 6.8×10^{19} cm^{-2}, (obtained from the online HEASoft tool for the GOODS-S coordinates) and adopted a redshifted $\log_{10}(N_{\mathrm{H}}/\mathrm{cm}^{-2})$ value of 24.5 to represent the typical observed value for ∼90% of Compton-thick AGN, where $24 < \log_{10}(N_{\mathrm{H}}) < 25$ brackets the minimum and maximum observed values (e.g., N. A. Levenson et al. 2006; N. A. Levenson 2014; E. S. Kammoun et al. 2019). For the input energy range, we used the observed X-ray flux range corresponding to the soft or hard band used in CSTACK, and entered the desired rest-frame energy range of 0.5–7 keV for the output energy. With the resulting stacked flux values from PIMMS, we converted to $L_{x,\mathrm{int}}$ using the luminosity distance corresponding to the average redshift of each redshift bin, and the k-correction value calculated using the Chandra CIAO tool *calc_kcorr* (https://cxc.cfa.harvard.edu/sherpa/ahelp/calc_kcorr.html) at the desired redshift and input/output energy range, via the following relation: $L_{\mathrm{X}} = F_{\mathrm{X}} \times 4\pi d_L^2 \times k(z)$.

Given that the CSTACK soft-band count rates are likely to be contaminated by host-galaxy emission, and/or a soft X-ray excess from the AGN, and/or extreme absorption, we chose for our final analysis to use only the stacked X-ray luminosities derived from the CSTACK hard-band count rates. This ensured that the stacked X-ray luminosities were being normalized by the AGN emission longward of ∼4 keV that should be minimally affected by these processes and therefore most accurately reflect the true intrinsic power-law emission of the AGN (see the AGN SED components in Figure 1 of R. C. Hickox & D. M. Alexander (2018), and the SEDs of minimally to highly obscured AGN in Figure 4 of that work, with a varying level of AGN dominance over the host galaxy). Furthermore, the stacked X-ray luminosities were calculated in a way that is consistent with the X-ray luminosities (J. Lyu et al. 2022) and associated N_{H} estimates (B. Luo et al. 2017) for the X-ray AGN sample to which they are compared in Figure 5: we adopt the same intrinsic power-law model and deabsorption assumptions (photoelectric and Thomson absorption only) to arrive at the intrinsic X-ray luminosity, with no scaling by a reflection efficiency.

3.3.2. X-Ray Luminosities and Specific Star Formation Rates

In Figure 5 we compare the average intrinsic X-ray luminosity, $L_{x,\mathrm{int}}$, of the mid-IR and X-ray AGN subsamples in different bins of LOS N_{H} obscuration. At the highest redshifts ($z > \sim 1.2$), we observe $L_{x,\mathrm{int}}$ peaking among the highly obscured X-ray AGN subset; and the stacked $L_{x,\mathrm{int}}$ for the mid-IR CT AGN lying nearly an order of magnitude lower. We also observe an unmistakable trend of the average $L_{x,\mathrm{int}}$ steadily decreasing through the X-ray AGN subsets with coincidentally decreasing obscuration (and also spatial asymmetry, A_S, as presented in Paper I). This picture mirrors the simulation results of S. McAlpine et al. (2020) who show that, at $z > 1$, ∼50% of BH activity triggered by major mergers occurs within a dynamical time after the active merging phase, in the postcoalescent remnant. Furthermore, they found that galaxies with the stellar ($M_* \sim 10^{10} M_\odot$) and black hole masses ($M_* < \sim 10^7 M_\odot$) typical of our sample show the greatest enhancement of BH activity from major mergers.

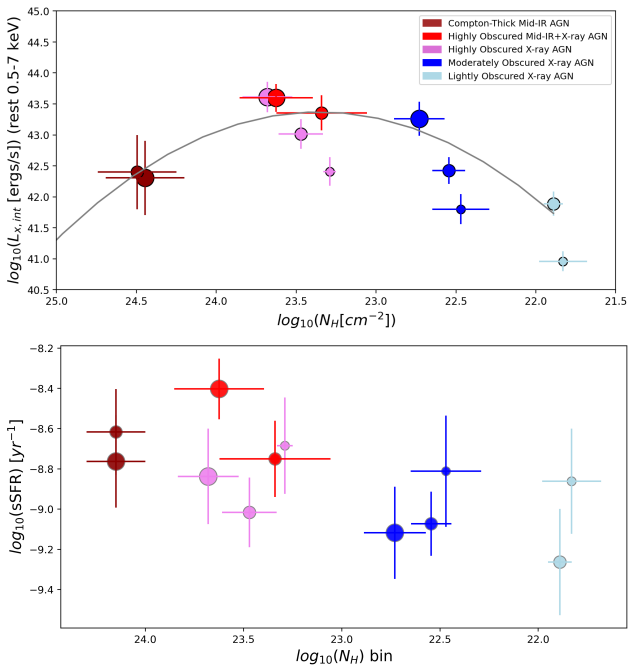

Figure 5. Median values of $L_{x,\mathrm{int}}$ and mass-normalized star formation rate (specific star formation rate, sSFR) versus N_{H} bin for the CT mid-IR/X-ray-faint AGN, X-ray/mid-IR-faint AGN, and small subset of AGN detected at both mid-IR and X-ray wavelengths, in multiple redshift bins (the $L_{x,\mathrm{int}}$ values for the mid-IR AGN represent the stacked values calculated as described in Section 4.1.1). Symbol sizes increase with redshift, where the smallest to largest points represent the redshift bins 0.5–1.2, 1.2–2.4, and 2.4–3.8. Error bars represent the median absolute deviation of values about the median value in each data bin. As discussed in Section 4.1.2, the trend plotted in the top figure, tracing the points of the two highest redshift bins, correlates with the trends of decreasing shape asymmetry and N_{H}, and therefore suggests a major-merger-driven Seyfert evolutionary sequence.

Similarly, the median mass-normalized star formation rates, sSFR, we measure track the expected trend of this property as a function of a major-merger timeline (e.g., as shown in the merger simulations of D. Sotillo-Ramos et al. 2022; A. L. Schechter et al. 2025): we observe the peak average sSFR coinciding with the most highly obscured X-ray AGN subset, along with $L_{x,\mathrm{int}}$, which bolsters our view that this may be a distinct Seyfert AGN phase marking the period of maximal accretion. While star formation in a subquasar AGN host galaxy can exist largely independently of the central BH activity, major-merger simulations of galaxies with stellar masses and morphologies similar to those characterizing our sample show that bursts of star formation predictably occur during pericentric passages prior to coalescence, and also with a delay after coalescence around the same time that the BH accretion rate also maximizes (S. Ellison et al. 2025; A. L. Schechter et al. 2025). This would indicate that the coincident peak of both $L_{x,\mathrm{int}}$ and SFR marks the window of time in which the predicted simultaneous bursts of AGN luminosity and star formation occur just prior to the AGN phase where feedback begins to counter the star formation activity and lower the measured SFR.

To complete the connection among these phases, R. C. Hickox et al. (2009) found that Spitzer/IRAC-detected infrared AGN lie mostly in the "blue cloud" while Chandra-detected X-ray AGN are more concentrated in the "green valley" with redder colors and a modest tendency toward higher optical luminosities and hence larger masses. These authors extensively compared and contrasted X-ray AGN and mid-IR AGN to reveal many similarities in their host galaxy properties in addition to their stellar colors, such as their clustering properties, suggesting they belong to the same population. This leads us to conclude that the CT-obscured mid-IR AGN and larger subsample of lightly to highly obscured X-ray AGN are not distinct AGN classes but related through major-merger evolution.[9]

Taken together, the average SED properties of the mid-IR and X-ray AGN samples suggest we are statistically likely to be witnessing the AGN emission footprint that characterizes an evolving major merger. Further support is lent to this interpretation from the observed features of the small subset of AGN with both X-ray and mid-IR emission, detected at $z > 1.2$. These systems exhibit similar peak values of $L_{x,\mathrm{int}}$ to the most highly obscured X-ray-bright/mid-IR-faint AGN, and have similar N_{H} levels but that extend to slightly lower levels. Given the minimal overlap between the X-ray and mid-IR AGN subsamples, meaning most of the X-ray AGN are undetected in the mid-IR and vice versa, this small fraction of AGN with both X-ray and mid-IR emission appears to represent a short-lived transitional phase between the two.

3.4. Comparison of AGN Trends with Inactive Control Sample

3.4.1. Control Sample Morphologies

We measured the spatial morphologies of the near-IR, mid-IR-, and X-ray-selected control samples using the same methodologies described in detail in Paper I, namely through human visual inspection and computer vision with the statmorph software. The former method involved qualitatively classifying each galaxy into one of the following morphological classes: point source, spheroid, disk (either symmetric/ordered, or mildly or strongly asymmetric/disturbed), irregular, and merger. For the latter method, we again adopted a conservative definition of $As \geqslant 0.3$ to define a strong host-galaxy disturbance, whereas M. M. Pawlik et al. (2016), who introduce A_S, define a strong disturbance as $As \geqslant 0.2$. We also split the AGN and control samples into two mass bins, 10^9–$10^{10}\,M_\odot$ and 10^{10}–$10^{11}\,M_\odot$, to observe any morphological trends with this property.

The results of the morphological analysis of the near-IR control sample revealed, for stellar masses between 10^{10} and $10^{11}\ M_\odot$, 9.4% strongly disturbed, as compared to 61% of AGN in the same mass range. The numbers come closer together for the lower-mass bin of 10^9–$10^{10}\,M_\odot$, meaning more disturbance is observed among the controls: 33% of the controls in this mass bin are strongly disturbed, compared with 70% of AGN. For the MIRI-selected control sample, a similar trend is observed: 84% of the CT mid-IR AGN exhibit strong spatial asymmetries at stellar masses between 10^9 and $10^{10}\ M_\odot$, compared to 35% for the MIRI-selected control galaxies; while for the stellar mass bin 10^9–$10^{10}\,M_\odot$, 59% of the AGN are highly disturbed and only 5% of the controls.

Overall, 29% of the MIRI inactive controls, 14% of the X-ray inactive controls, and 25% of the near-IR control sample are highly disturbed. A two-proportion z-test applied to each

[9] We note that comparisons with previous work (e.g., I. Georgantopoulos et al. 2023) must be done cautiously, since (1) this comparison could be affected by the presence of X-ray AGN in the red sequence, a population absent from the CT MIRI sample (R. C. Hickox et al. 2009) and (2) studies defining "obscured" through X-rays (e.g., C. Ricci et al. 2017; I. Georgantopoulos et al. 2023) miss the highest N_{H} bin entirely.

AGN sample and matched control shows, with strong confidence, that they are unlikely to be drawn from the same population, based on the following results (z statistic, two-sided p-value): $z = 8.97$, $p = 2.9 \times 10^{-19}$ for the mid-IR AGN and matched control sample, with a difference in proportions of 0.49 (95% CI 0.40–0.58); $z = 5.61$, $p = 2.0 \times 10^{-8}$ for the X-ray AGN and matched control sample, with a difference in proportions of 0.464 (95% CI 0.302–0.626); and $z = 11.24$, $p = 2.7 \times 10^{-29}$ for the full AGN sample and matched near-IR control sample, with a difference in proportions of 0.36 (95% CI 0.3–0.4).

As for morphological type, we observe that both the X-ray- and mid-IR-matched inactive control sample galaxies are mostly disks, mirroring the findings for the X-ray AGN, but different than the highly disturbed and irregularly shaped mid-IR AGN (see Figure 4 and Paper I). From this it is clear that the high degree and incidence of disordered morphologies characterizing the mid-IR AGN is unique to their nature as AGN (noting that the mid-IR control galaxies show a slightly higher fraction of irregular galaxies than the X-ray-selected control galaxies).

A comparison of the shape asymmetry values of all inactive controls to the simulated merging and nonmerging galaxies in N19 shows that they lie within the same approximate range as the nonmerging galaxies, all confined mostly to $0.1 < A_S < 0.3$. The simulated merging galaxies in that study and our AGN merger candidates overlap this A_S range but also significantly extend beyond to higher asymmetry values. If we take a conservative approach and consider all AGN in our sample with $A_S < 0.3$ as nonmergers, the results of Paper I remain, that a large fraction of our AGN sample are statistically highly disturbed. The study of the control sample morphologies presented here lends further support to our conclusion that, statistically, AGN are more likely to be involved in mergers than inactive galaxies.

4. Discussion

Our study spanning Papers I and II recovered and expanded upon the tentative result of J. L. Donley et al. (2018) that mid-IR-detected/X-ray-undetected AGN significantly reside in irregular, highly disturbed hosts appearing as merger remnants. Furthermore, it corroborated and extended to a higher redshift and level of N_H, the results of D. D. Kocevski et al. (2015), that a significant fraction of obscured X-ray-selected AGN at Cosmic Noon exhibit the galaxy-scale spatial disturbances associated with merging activity and that most have a disk morphology.

Our result is also in agreement with S. Ellison et al. (2025), who show that AGN incidence reaches a maximum shortly after coalescence, not in the precoalescent or early merging stage where a pair of nuclei is still visible. We note that their result is based on a number of AGN metrics, but does not include the heavily obscured stage, whereas our study tracks this trend to its logical end point in the CT mid-IR AGN subsample. Finally, our finding that mergers are associated with dust-obscured AGN is in agreement with the recent paper by A. La Marca et al. (2024) and the trend found by S. L. Dougherty et al. (2024).

4.1. Disk Morphologies of Merger Remnants

Until the release of Paper I, mergers were not considered to be a possible cause of disturbed disk morphology in AGN after coalescence, only before (e.g., D. D. Kocevski et al. 2015). This was based on hallmark early studies on AGN triggering mechanisms that indicated that mergers, particularly major mergers, would not result in a remnant with an ordered disk shape (J. Kormendy & R. C. Kennicutt 2004; P. F. Hopkins et al. 2006; P. F. Hopkins et al. 2014). However, as detailed in Paper I, numerous galaxy merger simulations have shown that disks commonly emerge from gas-rich major mergers, whether or not the interacting galaxies have a disk morphology before the merger. This powerful, relatively new understanding of the physics of galaxy mergers, in combination with our observation of significant signs of merger-induced disturbances in AGN host galaxies owing to the availability of JWST/NIRCam data, strongly supports a scenario in which subquasar Seyfert galaxies are evolving similarly to quasars at $z > \sim 0.5$ and $9 < \log(M_*/M_\odot) < 11$.

4.2. AGN Emerge in Early Postcoalescence

The X-ray emission of an AGN originates in its central engine, thus X-ray selection is sensitive to a broad range of evolutionary stages, excepting the most heavily obscured one. The infrared emission associated with the circumnuclear torus of dust and gas is nearly universal and also appears to be intrinsic. However, the infrared output associated with this embedding material fades as it is expelled by powerful winds and outflows from the central engine. As a result, the existence of a substantial population of heavily obscured, infrared-dominated AGN must represent a transitory stage relatively early in the life of the AGN, given that once the obscuring material is dispersed, it is inconceivable that it would be reassembled. This pins the highly obscured and spatially disordered mid-IR AGN in our sample to the late major-merger phase, given that the only physical process known to induce such a galaxy-wide spatial disruption and redistribution of gas and dust is a major merger. This then leaves two possibilities for the interpretation of the strongly disturbed disk morphologies that we have found in the X-ray obscured AGN: that they are either in the precoalescent or postcoalescent stage of a major merger. Given that it is not always possible to morphologically distinguish the pre- and postcoalescent phases of a merger due to degeneracies in their morphological properties (see N22 and our related discussion in Section 3), a search around each AGN within ~50 kpc for a nearby galaxy detected at the same redshift can achieve this goal. The fact that nearly all of the X-ray AGN in our sample appear isolated by this criterion leads us to conclude that they are largely in a postcoalescent phase.

This conclusion can be compared with the study of S. Ellison et al. (2025), who generated a sample of 21,235 galaxy pairs from the Sloan Digital Sky Survey DR7, 8141 postmerger systems from the Ultraviolet Near Infrared and Optical Northern Survey (UNIONS; S. Gwyn et al. 2025), and a large control sample of non-AGN galaxies. They used the Multi-Model Merger Identifier machine vision pipeline to determine a postmerger timeline for the galaxies and identify AGN through optical emission lines and the WISE W1 - W2 color. They found (see their Figure 4) a modest enhancement in AGN incidence premerger, with a much larger enhancement (by a factor of 3) just after coalescence, that persists at a lower level for 1 Gyr postmerger.

The time immediately postcoalescence is when interstellar clouds will have fallen into the potential well of the merged

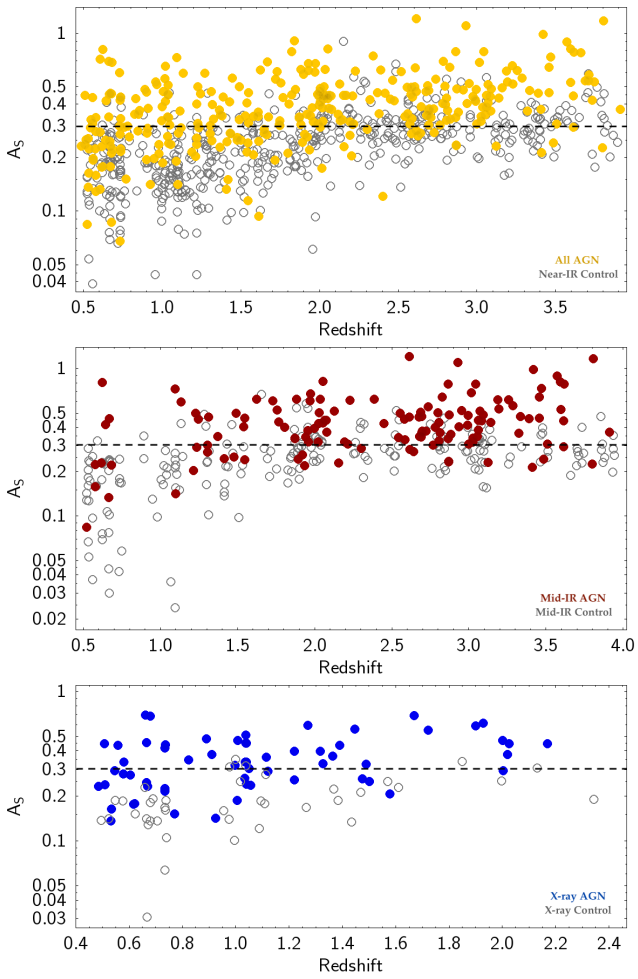

Figure 6. A comparison of the shape asymmetry distributions of the AGN subsamples and corresponding matched control samples. The top panel of the figure shows our full primary AGN sample (yellow, 66% with $A_S >= 0.3$) compared to the near-IR-selected control sample (25% with $A_S >= 0.3$); the middle panel shows the mid-IR AGN (red, 79% with $A_S >= 0.3$) and corresponding MIRI-selected control sample (29% with $A_S >= 0.3$); and the bottom panel shows the X-ray AGN (blue, 60% with $A_S >= 0.3$) compared to the X-ray-selected inactive control sample (14% with $A_S >= 0.3$). Here it can be seen that the majority of the property-matched inactive control galaxies exhibit A_S values largely confined to less than 0.35 (matching the A_S values and range of simulated nonmergers), while a significant fraction of the AGN extend to higher asymmetry values.

system and nuclear obscuration will be the strongest. Thus, any AGN activated during this period will tend to be embedded or strongly obscured and will be found preferentially in the infrared. This is exactly as in A. La Marca et al. (2024), who studied AGN and mergers in the Kilo Degree Survey (KiDS; J. T. A. de Jong et al. 2013); they found an excess of IR AGN by a factor of 2–3 in mergers, but only mild excesses for AGN identified through X-rays or SED analysis.

The infrared data used in these studies were not sufficiently deep and comprehensive to identify deeply embedded AGN, which are the subject of our study. The trends they find would be expected to be stronger for these more extreme infrared-identified AGN, consistent with our results. At the same time, the merger paradigm does not appear to apply to all AGN, as (1) we only observe mergers in our sample with statistical significance at $z > \sim 1$; and (2) Figure 6 shows that there is significant overlap between the shape asymmetry values for our AGN and control samples in the range of $A_S = 0.2$–0.3 (reminding the reader also that the simulated nonmerging galaxies of N19 show shape asymmetry values extending up to $A_S = 0.3$). That is, although we have found an association of mergers with obscured AGN, the evidence is still consistent with a significant subsample of AGN at $z < 1$ being fueled stochastically rather than in major mergers.

4.3. A Merger-driven Seyfert Evolutionary Scenario

On the basis of these results, we suggest an evolutionary scenario for the merger-induced branch of nuclear activity, depicted in Figure 7 in a style similar to the sketches in R. C. Hickox et al. (2009). We propose that the CT mid-IR AGN mark the early coalescence phase, where we necessarily expect to observe their descendants in the form of merger remnants, showing an initial increase in X-ray emission as the CT circumnuclear material begins to clear. As the remnant ages, we expect steadily diminishing levels of N_H, mid-IR emission, and spatial asymmetry as it reforms a disk shape after the merging event (D. Sotillo-Ramos et al. 2022 show that 58% of simulated major mergers among Milky Way- and M31-like galaxies reformed a destroyed disk shortly after the merger). In other words, as the most highly obscured X-ray AGN emerge from the CT mid-IR phase, their host galaxies settle into increasingly ordered and symmetric disk shapes with time past the merger event, where IR-emitting dust becomes increasingly confined to the disk and settles into a conventional circumnuclear torus. We believe this scenario to be the most likely to explain the set of host galaxy properties we measure for the X-ray AGN, as well as the relatively small number that are simultaneously detected in the mid-IR.

This is in agreement with the physical model of AGN feedback discussed in P. F. Hopkins & L. Hernquist (2006): due to their smaller, subquasar black hole masses, feedback in Seyferts is not expected to reach the most powerful "blowout" phase characterizing quasars; instead, it results in a weaker blast wave that fails to rapidly shut down host-galaxy star formation and result in the spheroid morphology characteristic of quasar remnants. This downsized version of quasar evolution appears to manifest as a population of AGN that (1) maintain, rapidly reform, or newly develop a gaseous disk morphology after a major merger; and (2) continue to form stars and feed the nucleus, with a steadily declining rate of BH accretion and star formation. This is how our X-ray AGN sample behaves.

In our comprehensive study of CT mid-IR and lightly to highly obscured X-ray AGN in Papers I and II, we have shown that these two apparently distinct types of AGN actually belong to the same AGN class, based on the observed morphological and AGN emission pattern appearing to connect them in a merger-driven evolutionary sequence. An additional piece of evidence that bolsters this conclusion is the finding that the dominant morphology of the mid-IR inactive control sample (mostly disks) differs from the matched mid-IR AGN sample (mostly irregular). In other words, if a high level of spatial disorder had been found to characterize both the non-AGN and AGN mid-IR-detected galaxies in our samples, then it would not be possible to attribute the highly disturbed and disordered morphologies of the mid-IR AGN to their nature as AGN. Likewise, the significant levels of disk disturbance observed in the X-ray AGN as compared to their non-AGN X-ray disk counterparts, allows us to firmly conclude that their

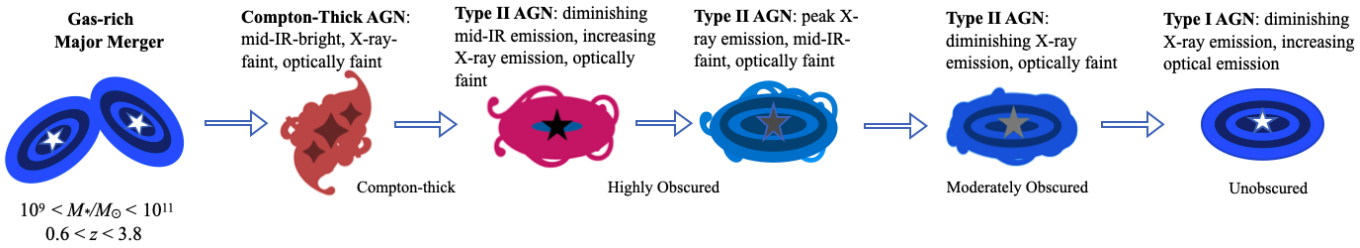

Figure 7. A second branch of the historically accepted Seyfert evolutionary sequence that allows for merging activity as a triggering mechanism, in addition to solely secular processes. This discovery among Cosmic Noon AGN host galaxies with $10^9 < M_*/M_\odot < 10^{11}$ and moderate AGN luminosities was enabled by the significant increase in spatial resolution and photometric sensitivity of JWST/NIRCam over its predecessor instruments, which allowed for the detection of a significant number and degree of merger-induced morphological disturbances.

morphologies are a result of their nature as merger-induced AGN.

Finally, it is remarkable, given our large AGN sample size that draws from ∼7 Gyr of cosmic history, that we do not witness a wide array of uncorrelated morphological and emission properties. Instead, we observe a correlation of properties that is consistent with that expected from an AGN evolving through a major merger, as opposed to the diverse signatures that would be anticipated from a mixture of unrelated triggering mechanisms.

5. Conclusions

Given the comprehensive morphological analysis of the large and representative sample of Seyferts we present in Paper I and here in Paper II, we conclude that the triggering of subquasar AGN at Cosmic Noon must in part be due to widespread merging, in tension with previously held beliefs that they only passively evolve. By comparing the morphologies and emission properties of CT mid-IR/X-ray-faint and X-ray-bright/mid-IR-faint AGN subsamples, we find that they represent distinct phases of a merger-driven evolutionary sequence, as opposed to distinct AGN classes. The various lines of evidence in support of this theory have been laid out in Paper I and the current paper, and is most convincing when comparing the AGN host-galaxy properties to an inactive control sample presented here in Paper II: the pattern of morphological disturbances and types observed among the AGN sample is not found in the large sample of inactive controls. Therefore, we are left to conclude that the high level of disturbance and irregularity of the mid-IR AGN is due to their being late-stage mergers; and likewise, that the high fraction of disturbed disk morphologies observed among the X-ray AGN translates to them being the postmerger remnants with steadily decreasing X-ray luminosities and levels of obscuration as they evolve in time past the merger event.

Acknowledgments

This work was supported by NASA grants NNX13AD82G, 1255094, and the NASA contract for NIRCam to the University of Arizona, NAS5-02015. The research of C.J.W. was enabled by grant 18JWST-GTO1 from the Canadian Space Agency and funding from the Natural Sciences and Engineering Research Council of Canada. N.B. and C.N.A.W. acknowledge support from the NIRCam Science Team contract to the University of Arizona, NAS5-02015. J.L. and G.H.R. acknowledge support from the JWST Mid-Infrared Instrument (MIRI) Science Team Lead, grant 80NSSC18K0555, from NASA Goddard Space Flight Center to the University of Arizona. A.J.B. acknowledges funding from the "FirstGalaxies" Advanced grant from the European Research Council (ERC) under the European Union's Horizon 2020 research and innovation program (grant agreement No. 789056). This work is based on observations made with the NASA/ESA/CSA James Webb Space Telescope. These observations are associated with JWST GTO programs #1180, #1181, and #1207, and GO program #1963.

Facilities: JWST, CXO.

Appendix

We have used the LOS N_H as a proxy for the degree to which an AGN is embedded. This overlooks the issue that the material around an AGN is distributed anisotropically, so there is an uncertainty term in our placement of sources in ranges of obscuration. This issue is quantified by the covering fraction, the fraction of the sky seen by the central engine that contains the obscuring material. Estimates of this parameter are summarized by G. Hasinger (2008, H08), who shows it is a function of AGN luminosity; in the range of the Seyfert-like sources we are studying, it is of order ∼70% (see H08 Figure 7). More recent models are in good agreement: (1) C. Ricci et al. (2017) have modeled the behavior of sources in the Swift/BAT 70 month AGN Catalog, finsing that for those with $N_H > 0.5 \times 10^{22}$ cm^{-2}, the average covering fraction is about 65%. (2) L. Lanz et al. (2019) also analyzed Swift/BAT measurements, supplemented with data from Herschel and NuStar; they deduced average covering fractions of 70%–80%. When comparing with other determinations, one should beware of the strong luminosity dependence shown by H08 and avoid inclusion of sources above the luminosity range of our sample.

The effects of anisotropic obscuration are discussed below for two different cases: (1) the most heavily obscured, infrared-only AGN; and (2) the less obscured, X-ray detected ones.

Appendix A
Dust Torus Covering Fraction in Infrared-only AGN

The H08 result is dominated by relatively lightly obscured AGN, showing that, as the obscuration increases, the covering fraction tends to grow and the dustiness of the central engine environment increases. Here we quote other studies that support this result. (1) M. Brightman & Y. Ueda (2012): "We find that the covering factor of the circumnuclear material is correlated with the LOS column density NH, and as such the most heavily obscured AGN are in fact also the most geometrically buried.... We find that a significant fraction of sources (∼20 per cent) in the CDFS are likely to be buried in

material with close to 4π coverage having been best fitted by the torus model with a 0° opening angle." (2) C. Ricci et al. (2021): "The vast majority (85^{+7}_{-9}%) of the AGN in the final merger stages ($d_{\rm sep} \leqslant 10$ kpc) are heavily obscured ($N_{\rm H} \geqslant 10^{23}$ cm^{-2}), and the median $N_{\rm H}$ of the accreting SMBHs in our sample is systematically higher than that of local hard X-ray-selected AGN, regardless of the merger stage. This implies that these objects have very obscured nuclear environments, with the $N_{\rm H} \geqslant 10^{23}$ cm^{-2} gas almost completely covering the AGN in late mergers."

We now extend this argument to sources identified as AGN from the infrared properties alone, without X-ray detection. For these, we need to extrapolate to an appropriate typical covering fraction. We have done so in the following steps: (1) we take all CT AGN listed either in C. E. Goldberg et al. (2024) or in the Swift/BAT survey (M. Ajello et al. 2012), with [Ne V] λ 14.32 μm line strengths from M. Pereira-Santaella et al. (2010) and infrared photometry from WISE. Both the W3 (12 μm) and [Ne V] fluxes should be rough indicators of total luminosity (L. Spinoglio et al. 2022 and L. Spinoglio et al. 2024, respectively). The 12 μm flux has been shown to be a relatively good indicator of isotropic obscuration in a number of studies (e.g., S. M. LaMassa et al. 2010). [Ne V] is emitted in the narrow-line region (NLR) and is not strongly affected by extinction; therefore, it reaches the observer from regions above the circumnuclear torus, i.e., it should also be an indicator of isotropic obscuration. We compare the ratio of these two luminosity indicators with the steepness of the infrared SED, with the following motivation: if the [Ne V]/12 μm ratio decreases as the SED "redness" increases, it implies that less of the nuclear flux is escaping to excite [Ne V], and therefore that the covering fraction is large. For a comparison sample we used all AGN of Type 1–1.5 listed in M. Pereira-Santaella et al. (2010) with [Ne V] line measurements with adequate signal-to-noise ratios.

The result is shown in Figure 8: increasingly red infrared SEDs correlate with decreasing ratios of [Ne V]/12 μm. This indicates that cases with extreme infrared excesses tend to allow relatively less nuclear light to escape into their NLRs, consistent with their having larger covering fractions than less-embedded cases, like the AGN 1–1.5 shown in the figure. Given that Figure 8 shows a reduction in escaping light by a factor of 2 more for the most-obscured cases, the suggestion is that the high-redshift, IR-only AGN are likely to have covering fractions larger than the usual 65%–80% for typical cases, more on order of 85%–90%.

We finally consider the effects of nonisotropic obscuration on our results. P. G. Boorman et al. (2025) estimate that low-obscuration regions typically have a 1.4 dex lower $N_{\rm H}$ column density than the LOS $N_{\rm H}$ indicated for a high obscuration region. We calculate on the basis that 85% of the AGN is covered at the measured LOS $N_{\rm H}$, and 15% is 1.4 dex less obscured. The average obscuration is then reduced by 14% from that deduced from assuming that the LOS $N_{\rm H}$ applies isotropically, i.e., there is no effect on our results. There is a second issue, that 10%–15% of the most-obscured cases will (if they have X-ray detections) appear to be at an obscuration 1 dex too low (P. G. Boorman et al. 2025). Again, this has no impact on our results.

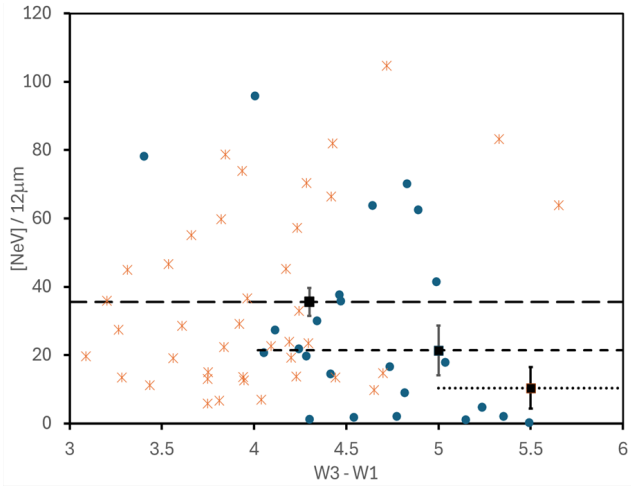

Figure 8. The ratio of [Ne V] λ 14.32 μm strength (in W m^{-2}) to 12 μm flux density (in Jy) vs. the W1 − W3 color. The star symbols represent Type 1–1.5 AGN and the circular symbols represent CT AGN. The broad dashed line is the average for the Type 1 galaxies, while the narrower dashed line is for CT cases with W3 − W1 > 4, and the dotted line is the average for the CT cases with W3 − W1 > 5.

Appendix B
Dust Torus Covering Fraction for Less-obscured AGN

We treat the less-obscured cases in a parallel fashion. We assume 70% coverage, with the remaining 30% showing reduced obscuration by 1.4 dex. In this case, the true obscuration is 71% of that deduced from taking the observed LOS $N_{\rm H}$ to be isotropic. It is also the case that ∼30% of AGN with a given isotropic obscuration will appear to have $N_{\rm H}$ 1.4 dex too low. From Paper I, the distribution of $N_{\rm H}$ is constant for our sample between 10^{22} and 10^{24} cm^{-2}, so our results in this $N_{\rm H}$ range will be somewhat blurred across $N_{\rm H}$ lines. However, in a statistical sense they should remain valid.

ORCID iDs

Nina Bonaventura https://orcid.org/0000-0001-8470-7094
George H. Rieke https://orcid.org/0000-0003-2303-6519
Jianwei Lyu (吕建伟) https://orcid.org/0000-0002-6221-1829
Andrew J. Bunker https://orcid.org/0000-0002-8651-9879
Chris J. Willott https://orcid.org/0000-0002-4201-7367
Christopher N. A. Willmer https://orcid.org/0000-0001-9262-9997

References

Ajello, M., Alexander, D. M., Greiner, J., et al. 2012, ApJ, 749, 21
Annuar, A., Alexander, D. M., Gandhi, P., et al. 2025, MNRAS, 540, 3827
Barrows, R. S., Comerford, J. M., Stern, D., et al. 2023, ApJ, 951, 92
Bonaventura, N., Lyu, J., Rieke, G. H., et al. 2025, ApJ, 978, 74
Boorman, P. G., Gandhi, P., Buchner, J., et al. 2025, ApJ, 978, 118
Brightman, M., & Ueda, Y. 2012, MNRAS, 423, 702
Bruzual, G., & Charlot, S. 2003, MNRAS, 344, 1000
Burtscher, L., Davies, R. I., Graciá-Carpio, J., et al. 2016, A&A, 586, A28
Ciesla, L., Charmandaris, V., Georgakakis, A., et al. 2015, A&A, 576, A10
Conselice, C. J., Mundy, C. J., Ferreira, L., et al. 2022, ApJ, 940, 168
de Jong, J. T. A., Verdoes Kleijn, G. A., Kuijken, K. H., et al. 2013, ExA, 35, 25
Donley, J. L., Kartaltepe, J., Kocevski, D., et al. 2018, ApJ, 853, 63
Donley, J. L., Koekemoer, A. M., Brusa, M., et al. 2012, ApJ, 748, 142

Dougherty, S. L., Harrison, C. M., Kocevski, D. D., et al. 2024, MNRAS, 527, 3146
Ellison, S., Ferreira, L., Bickley, R., et al. 2025, OJAp, 8, 12
Ellison, S. L., Viswanathan, A., Patton, D. R., et al. 2019, MNRAS, 487, 2491
Euclid Collaboration, La Marca, A., Wang, L., et al. 2025, arXiv:2503.15317
Florian, M. K., Rieke, G. H., Alberts, S., et al. 2025, ApJ, 990, 102
Gao, F., Wang, L., Pearson, W. J., et al. 2020, A&A, 637, A94
Georgantopoulos, I., Pouliasis, E., Mountrichas, G., et al. 2023, A&A, 673, A67
Getman, K. V., Feigelson, E. D., Broos, P. S., et al. 2010, ApJ, 708, 1760
Goldberg, C. E., Buiten, V. A., Rieke, G. H., et al. 2024, ApJ, 977, 55
Goulding, A. D., Greene, J. E., Bezanson, R., et al. 2018, PASJ, 70, S37
Grazian, A., Fontana, A., de Santis, C., et al. 2006, A&A, 449, 951
Gwyn, S., McConnachie, A. W., Cuillandre, J.-C., et al. 2025, AJ, 170, 324
Hasinger, G. 2008, A&A, 490, 905
Hickox, R. C., Jones, C., Forman, W. R., et al. 2009, ApJ, 696, 891
Hickox, R. C., & Alexander, D. M. 2018, ARA&A, 56, 625
Hopkins, P. F., & Hernquist, L. 2006, ApJS, 166, 1
Hopkins, P. F., & Hernquist, L. 2009, ApJ, 694, 599
Hopkins, P. F., Kocevski, D. D., Bundy, K., et al. 2014, MNRAS, 445, 581
Hopkins, P. F., Somerville, R. S., Hernquist, L., et al. 2006, ApJ, 652, 864
Kammoun, E. S., Miller, J. M., Koss, M., et al. 2020, ApJ, 901, 161
Kammoun, E. S., Miller, J. M., Zoghbi, A., et al. 2019, ApJ, 877, 102
Kim, D., Kim, Y., Im, M., et al. 2024, A&A, 690, A283
Kocevski, D. D., Brightman, M., Nandra, K., et al. 2015, ApJ, 814, 104
Kormendy, J., & Kennicutt, R. C., Jr. 2004, ARA&A, 42, 603
La Marca, A., Margalef-Bentabol, B., Wang, L., et al. 2024, A&A, 690, A326
LaMassa, S. M., Heckman, T. M., Ptak, A., et al. 2010, ApJ, 720, 786
Lanz, L., Hickox, R. C., Baloković, M., et al. 2019, ApJ, 870, 26
Lehmer, B. D., Basu-Zych, A. R., Mineo, S., et al. 2016, ApJ, 825, 7
Levenson, N. A. 2014, IAUS, 304, 112
Levenson, N. A., Heckman, T. M., Krolik, J. H., et al. 2006, ApJ, 648, 111
Liu, T., Tozzi, P., Wang, J.-X., et al. 2017, ApJS, 232, 8
Luo, B., Brandt, W. N., Xue, Y. Q., et al. 2017, ApJS, 228, 2
Lyu, J., Alberts, S., Rieke, G. H., et al. 2022, ApJ, 941, 191
Lyu, J., Alberts, S., Rieke, G. H., et al. 2024, ApJ, 966, 229
McAlpine, S., Bower, R. G., Rosario, D. J., et al. 2018, MNRAS, 481, 3118
McAlpine, S., Harrison, C. M., Rosario, D. J., et al. 2020, MNRAS, 494, 5713
Miyaji, T., Griffiths, R. E. & C-COSMOS Team 2008, AAS, 10, 4.01
Nevin, R., Blecha, L., Comerford, J., et al. 2019, ApJ, 872, 76
Nevin, R., Blecha, L., Comerford, J., et al. 2023, MNRAS, 522, 1
Omori, K. C., Bottrell, C., Bellstedt, S., et al. 2025, ApJ, 989, 73
Padovani, P., Alexander, D. M., Assef, R. J., et al. 2017, A&ARv, 25, 2
Pawlik, M. M., Wild, V., Walcher, C. J., et al. 2016, MNRAS, 456, 3032
Pereira-Santaella, M., Diamond-Stanic, A. M., Alonso-Herrero, A., et al. 2010, ApJ, 725, 2270
Pfeifle, R. W., Satyapal, S., Secrest, N. J., et al. 2019, ApJ, 875, 117
Puskás, D., Tacchella, S., Simmonds, C., et al. 2025, MNRAS, 540, 2146
Ricci, C., Bauer, F. E., Treister, E., et al. 2017, MNRAS, 468, 1273
Ricci, C., Privon, G. C., Pfeifle, R. W., et al. 2021, MNRAS, 506, 5935
Rieke, G. H., Sun, Y., Lyu, J., et al. 2025, ApJ, 994, 35
Rieke, M. J., Robertson, B., Tacchella, S., et al. 2023, ApJS, 269, 16
Risaliti, G., Maiolino, R., & Salvati, M. 1999, ApJ, 522, 157
Rodriguez-Gomez, V., Snyder, G. F., Lotz, J. M., et al. 2019, MNRAS, 483, 4140
Santini, P., Maiolino, R., Magnelli, B., et al. 2014, A&A, 562, A30
Schechter, A. L., Genel, S., Terrazas, B., et al. 2025, ApJ, 989, 149
Shah, E. A., Kartaltepe, J. S., Magagnoli, C. T., et al. 2020, ApJ, 904, 107
Shi, Y., Rieke, G., Lotz, J., et al. 2009, ApJ, 697, 1764
Sotillo-Ramos, D., Pillepich, A., Donnari, M., et al. 2022, MNRAS, 516, 5404
Spinoglio, L., Fernández-Ontiveros, J. A., & Malkan, M. A. 2022, ApJ, 941, 46
Spinoglio, L., Fernández-Ontiveros, J. A., & Malkan, M. A. 2024, ApJ, 964, 117
Villforth, C. 2023, OJAp, 6, 34
Weigel, A. K., Schawinski, K., Treister, E., et al. 2018, MNRAS, 476, 2308
Weston, M. E., McIntosh, D. H., Brodwin, M., et al. 2017, MNRAS, 464, 3882
Williams, C. C., Tacchella, S., Maseda, M. V., et al. 2023, ApJS, 268, 64
Wright, E. L., Eisenhardt, P. R. M., Mainzer, A. K., et al. 2010, AJ, 140, 1868
Zhao, Y., Li, Y. A., Shangguan, J., et al. 2022, ApJ, 925, 70